# Promoting effect of oxygen vacancies in Co/CoAl$_2$O$_4$ catalyst steered with a straightforward method on hydrogenation of furfural to 2-methylfuran

Yongwang Li [a], Qi Shen [a], Yao Nian [a], Fumin Wang [a,b,*], Xubin Zhang [a,**], Zhengliang Zhang [a], Changhao Bing [a], Xiaolu Fan [a], Rosine Ahishakiye [a]

[a] School of Chemical Engineering and Technology, Tianjin University, Tianjin 300350, PR China
[b] Tianjin Key Laboratory of Applied Catalysis Science and Engineering, Tianjin University, Tianjin 300350, PR China

ARTICLE INFO

ABSTRACT

The exploitation of base metal catalysts to upgrade biomass chemicals remains a daunting challenge and a sustainable strategy. Here, a series of Co-Al spinel catalysts are rapidly prepared by low-temperature solution combustion synthesis for hydrogenation of furfural (FF) to 2-methylfuran (2-MF), in which oxygen vacancies are easily manipulated by regulating the proportion of glycine in the ingredients. The screened Co/CoAl$_2$O$_4$ incorporating adequate oxygen vacancies yields 2-MF over 97 % at 150 °C for 5 h, rivalling the state-of-the-art catalysts to date. Characterizations and DFT calculations attribute the success to oxygen vacancies, which not only enhance the adsorption of FF by changing the adsorption geometry, but also facilitate the hydrogen spillover from Co to substrate by moving down the *d*-band center of CoAl$_2$O$_4$. This study provides a versatile methodology for the efficient and low-temperature preparation of spinel and the construction of defect engineering on catalysts, enlightening the design of phenomenal catalysts.

## 1. Introduction

The hydrodeoxygenation of renewable biomass represented by FF provides a new approach to alleviate global energy shortage [1–5]. Among them, the selective conversion of FF into versatile and high value-added 2-MF has become a current research hotspot [6–8]. Despite many excellent noble metal catalysts have been developed, which are restricted in their application due to high usage costs and scarce resources, it is of great industrial significance to design efficient base metal catalysts for catalytic hydrogenation of FF to 2-MF [9–11].

Base metals such as Co, Ni and Cu have been widely studied in the hydrodeoxygenation of FF, and the catalytic activities are improved by means of doping heteroatoms (Cu-Cu$_2$O/N-RGO, CuSi-N, Co-900) [12–14], metal compounding (Co-Mo/Al$_2$O$_3$, NiCuAl, CoCuAl, NiMo IMC) [15–17], metal-support interactions (Cu-Ni/TiO$_2$) [18], etc. Nevertheless, Ni promotes C≡C hydrogenation through its stronger binding ability with the furan ring of FF, which reduces the selectivity for 2-MF;[19,20] Cu affords a weak dissociation ability to H$_2$, limiting its catalytic activity [17,21]. Among all base metals, Co nanoparticles exhibit excellent catalytic activity and stability in the hydrogenation of

biomass based compounds containing functional groups such as aldehyde, ketone, and carboxyl groups [14,22]. Moreover, CoO$_x$ can induce the hydrogenolysis of C-OH [23–25]. Meanwhile, Al species can provide abundant acidic sites and serve as a stable catalyst framework, which are crucial for the hydrogenolysis step [25,26]. Therefore, the combination of Co and Al can facilitate the hydrodeoxygenation of FF to 2-MF.

Lewis acid plays a crucial role in the hydrogenation of FF, with the most common being metal oxides [27]. Accordingly, monometallic oxides such as TiO$_2$, Al$_2$O$_3$, and ZrO$_2$ are often used as catalyst supports [10,15,28,29]. Distinguished from monometallic oxides, spinel oxides with superior versatility, flexible ion arrangement, and multivalent structure show excellent catalytic activity, which makes them widely studied in the hydrogenation of FF [30,31]. Using LDHs as the precursor to synthesize spinel oxides is a common method, and the preparation of LDHs by in situ hydrothermal method or coprecipitation method ensures the uniform dispersion of metal species, but the precise pH regulation, tedious steps and lengthy growth time are major obstacles to the synthesis process [32]. In contrast, solution combustion synthesis (SCS) process relying on self-sustained exothermic effect can efficiently obtain high crystallinity spinel oxides at lower temperatures, yet limited

---

research exists in the field of biomass hydrogenation [33].

Benefiting from abundant *d* electrons and empty *d*-orbitals, noble metals have always outperformed base metals in catalytic hydrogenation reactions. To break free from shackles so as to match the catalytic activity of noble metals, many methods have been used to enhance the density of the electron cloud around the base metals and regulate their *d*-band centers, among which the construction of carrier vacancies has been proven feasible, especially oxygen vacancy ($V_O$) [34]. For example, the doping of Na and oxygen vacancies in the $RuO_2$ catalyst weakens its adsorption strength with the intermediate by lowering the *d*-band center, thereby weakening the barrier of oxygen evolution reaction (OER) [35]. Defect-engineering strategy is implemented to construct ultrathin δ-$MnO_2$ nanosheets with abundant oxygen vacancies, which generates more $Mn^{3+}$ and stronger water adsorption capacity, contributing to robust performance for both hydrogen evolution reaction (HER) and OER [36]. In the process of Co@CoO catalyst converting 5-hydroxymethylfurfural (HMF) to 2,5-dimethylfuran (DMF), oxygen vacancies not only motivate the heterolytic cleavage, but also catalyze the homolytic splitting of $H_2$ [37]. In the simulated reaction of Pt@$TiO_{2-x}$ catalyzing hydrogenation of aldehyde group, the further hydrogenation of interfacial OH* intermediates becomes thermodynamically and kinetically effective due to the oxygen vacancy, which realizes the synergistic catalytic hydrogenation [38]. Taking inspiration from this, the method of introducing oxygen vacancies into metal oxides is established to ameliorate their intrinsic catalytic performance.

Herein, a series of spinel catalysts rich in oxygen vacancies are efficiently synthesized in a short period of time by simply adjusting the doping ratio of glycine (Gly). The Co/$CoAl_2O_4$ catalyst exhibits excellent catalytic performance for the hydrodeoxygenation of FF to 2-MF, with a 2-MF yield of over 97 % rivalling noble metal catalysts. Detailed characterizations and density functional theory (DFT) calculations ascribe the significant catalytic activity to the synergistic effect between an abundance of oxygen vacancies and vicinal Co active sites on the surface of $CoAl_2O_4$-$V_O$. Sufficient oxygen vacancies enhance the adsorption of FF and intermediate product furfuryl alcohol (FOL), and facilitate the hydrogen spillover from Co to organic molecules by moving down the *d*-band center of $CoAl_2O_4$. This green and efficient defect construction strategy guides new ideas for the development of hydrogenation catalysts.

## 2. Experimental section

### 2.1. Materials

Co$(NO_3)_2$·6 $H_2O$ (purity 99 %) and Al$(NO_3)_3$·9 $H_2O$ (purity 99 %) were purchased from Shanghai Aladdin Biochemical Technology Co., Ltd. Glycine (purity 98 %) was purchased from Tianjin Heowns Biochem LLC. Furfural (purity 99 %) and furfuryl alcohol (purity 99 %) were purchased from Meryer (Shanghai) Chemical Technology Co., Ltd. 5-hydroxymethylfurfural (purity 99 %) was purchased from Tianjin Heowns Biochem LLC. Anhydrous ethanol (purity AR) was purchased from Real&Lead Chemical Co., Ltd. $H_2$ gas (purity 99.99 %) was purchased from Tianjin Liufang Industrial Gas Co., Ltd. All the reagents were used without further purification.

### 2.2. Catalyst synthesis

All catalysts with different Co:Al:Gly ratios were synthesized through solution combustion synthesis method. In a typical synthesis, 0.0075 mol of Co$(NO_3)_2$·6 $H_2O$ and 0.0075 mol of Al$(NO_3)_3$·9 $H_2O$ were dissolved in 2 mL of deionized water and stirred at 60 ℃ water bath for 30 min. Next, 0.0105 mol of Gly was added and the temperature was raised to 80 ℃. After an hour of stirring, the mixture became a purple viscous substance, and most of the water had already evaporated. After transferring the viscous substance to an oven at 170–180 ℃ and heating it for about 90 min, a combustion reaction occurred, accompanied by the

generation of gray black powder, named Co/$CoAl_2O_4$-UR. The gray black powder was reduced under a 10 % $H_2$/90 % Ar mixture (80 mL/min) at 500 ℃ for 2 h with a heating rate of 5 ℃/min to form Co/$CoAl_2O_4$. Co/$CoAl_2O_4$-R400 and Co/$CoAl_2O_4$-R600 were synthetized by adjusting the reduction temperature to 400 and 600 ℃, respectively. With the total molar quantity of the metal precursors and other conditions unchanged, 0.4Co/0.6Al-Co/$CoAl_2O_4$ and 0.6Co/0.4Al-Co/$CoAl_2O_4$ were obtained by adjusting the $n_{Co}/n_{Al}$ ratio in the precursors to 0.4:0.6 and 0.6:0.4. Similarly, 0.6Gly-Co/$CoAl_2O_4$ and 0.8Gly-Co/$CoAl_2O_4$ were synthesized by adjusting the amount of Gly according to the $n_{Gly}/(n_{Co}+n_{Al})$ ratio of 0.6 and 0.8.

### 2.3. Characterization

X-ray diffraction (XRD) was conducted on a Bruker D8 ADVANCE X-ray (40 mA, 40 kV) using Co Kα radiation at a scanning rate of 8°/min in the 2θ range of 5–120°, and the test results (Co Kα radiation, $\lambda_{Co}$ = 1.79026 Å) are converted into corresponding data with Cu target anode (Cu Kα radiation, $\lambda_{Cu}$ = 1.54060 Å) through the Bragg equation. Textural parameters of all catalysts were collected by low-temperature $N_2$ adsorption/desorption experiments using a SSA-7000 instrument, which were degassed at 150 ℃ for 4 h and gauged at − 196 ℃. Inductive Coupled Plasma (ICP-OES/MS, Agilent 725ES & 5110OES, America) was applied to analyze the content of various metals in the catalysts.

Scanning electron microscopy (SEM, Apreo S, Czech Republic) and transmission electron microscopy (TEM, JEM-2100 F, Japan) were performed to survey the distribution of metal particles on the surfaces of these samples. High-resolution transmission electron microscope (HRTEM) images, elemental mapping images and selected area electron diffraction (SAED) patterns were obtained on a field emission transmission electron microscope (HRTEM, JEM-F200, Japan) to observe the elemental distribution and exposed crystal planes on the catalyst surface.

X-ray photoelectron spectroscopy (XPS) spectra was recorded on an Axis Supra equipment to measure the valence state of Co and O on the surfaces of the catalysts, which were exposed to air before outgassing in the spectrometer, and the binding energy was calibrated by the C 1 *s* line of contaminated carbon (284.8 eV). Oxygen vacancies were analyzed by electron paramagnetic resonance (EPR, Bruker A300, Germany) at 77 k using TEMPO as the spin-trapping agent. Temperature-programmed desorption (TPD) experiments were carried out on an AutoChem1 II 2920 equipment to analyze the hydrogen spillover in each sample. After degassing 200 mg of the catalyst at 150 ℃, 10 % $H_2$/Ar mixture (30 mL/min) was imported into the reactor at 50 ℃ for 1 h to saturate catalyst adsorption. Subsequently, 10 % $H_2$/Ar mixture was switched to Ar for 1 h to remove $H_2$ physically adsorbed on the surface of the catalyst. TCD detection data were collected with the desorption temperature increasing from 50 ℃ to 650 ℃ at a rate of 10 ℃/min under Ar atmosphere thereafter. The pyridine-adsorbed diffuse reflectance infrared Fourier transform (pyridine-DRIFT) spectra were recorded on a Frontier spectrometer (PerkinElmer, USA) to analyze the acidic nature and strong acid content of the catalysts. 25 mg of the sample was pressed into a circular disc with a diameter of 13 mm and placed in the in-situ cell degassing for 1 h under Ar atmosphere at 350 ℃. Next, pyridine was injected at 150 ℃ for 0.5 h to bind with acidic sites on the surface of the sample. After Ar gas introduced for another 1 h to remove weakly adsorbed pyridine on the surface of the sample, DRIFT spectra were recorded at 200 and 350 ℃, respectively. FT-IR (Nicolet 380, America) was used to characterize the adsorption configuration of FF and FOL on the surfaces of the catalysts. The preparation steps of the samples are as follows: 20 μL of FF or FOL were dropwise added to 10 mg of the catalyst, which was heated at 150 ℃ under $N_2$ (60 mL/min) for 1 h to remove the physically adsorbed reactants on the surface, and then mixed with KBr for tablet pressing.

## 2.4. Catalytic evaluations

A 200 mL stainless steel autoclave was used to evaluate the performance of the catalysts for furfural hydrogenation. Before importing $H_2$ to purge the reactor, 0.1 g of the catalyst, 1 g of furfural, and 19 g of anhydrous ethanol were added to the autoclave. After three times purification, the reactor was pressurized to 1.5 MPa and heated to 150 ℃ for 30 min upon stirring at 600 rmp. After 5 h of reaction, the reactor was rapidly chilled to room temperature in a water bath. After centrifuging the mixed product, 0.3 μL of the liquid phase products were injected into a gas chromatography (Beifen-Ruili, 3420 A) with a KB-WAX capillary column (30 m × 0.32 mm × 0.50 μm) to analyze product distribution. Furfural conversion ($X_F$) and selectivity to products ($S_i$) were calculated by Eqs. (1) and (2):

$$X_F = \left(1 - \frac{\varphi_F}{\varphi_{F0}}\right) \times 100\% \tag{1}$$

$$S_i = \left(\frac{\varphi_i}{1 - \varphi_F}\right) \times 100\% \tag{2}$$

Where $\varphi_F$ represents the molar amount of FF after the reaction, $\varphi_{F0}$ represents the initial molar amount of FF, and $\varphi_i$ represents the molar amount of products (FOL, 2-MF, etc.).

After the reaction, the catalyst was obtained by centrifugation and washed with ethanol three times. The catalyst was then dried in a vacuum oven at 50 ℃ for 6 h for the next reaction. During the recycling process, the catalyst lost about 20 %, and the lost part was supplemented with the fresh catalyst.

The ability of the catalyst to catalyze the hydrogenation of 5-hydroxymethylfurfural was evaluated by replacing furfural with a certain amount of 5-hydroxymethylfurfural, with other conditions unchanged.

The carbon balance of all reactions in this study is above 93 %.

## 2.5. Computational details

Energetics calculations for adsorption were fulfilled by using spin-polarized density functional theory with generalized gradient approximation (GGA) and Perdew-Burke-Ernzerhof (PBE) as implemented in VASP 5.4.4 [39–42]. To eliminate the interaction between adjacent periodic units in the z-direction, the vacuum layer was set to 15 Å. A Co (111)-p(2 ×2) surface slab was applied to model the Co particle with cell parameters of a = 9.74 Å, b = 8.44 Å, and c = 22.96 Å. A Co(200)-p (3 ×3) surface slab was applied to model the Co particle with cell parameters of a = 10.34 Å, b = 10.34 Å, and c = 21.89 Å. A CoAl$_2$O$_4$(311)-p(1 ×1) surface slab was conducted to model the substrate with cell parameters of a = 19.89 Å, b = 11.49 Å, and c = 21.26 Å. The bottom two layers of atoms in the structures of Co(111), Co(200), and CoAl$_2$O$_4$(311) catalysts were fixed, while the remaining atoms were allowed to relax. For structural optimization of Co(111) and Co(200), the cutoff energy of plane-wave basis set was set as 350 eV and the Brillouin zone was sampled with a 2 × 2 × 1 k-point grid. Since the oxide model has more than 150 atoms, the cutoff energy of plane-wave basis set was set as 500 eV and single gamma-point grid sampling was used for Brillouin zone integration. Atomic positions were optimized until the forces were less than 0.02 eV/Å. The adsorption energy of an adsorbate ($E_{ad}$) was calculated using Eq. (3):

$$E_{ad} = E_{ad-state} - E_{cat} - E_{adsorbate} \tag{3}$$

where $E_{ad-state}$, $E_{cat}$, and $E_{adsorbate}$ refer to the adsorption energy of the catalyst with adsorbate, the catalyst and adsorbate, respectively.

To investigate the effect of solvents on adsorption energy, the VASPsol code was implemented to simulate the solvent environment, with the relative permittivity of ethanol set to 28.4 [43,44]. The VASPKIT code was employed for thermodynamic correction of adsorption energy at 423.15 K [45].

## 3. Results and discussion

### 3.1. Catalyst characterization

Fig. 1a shows the process of preparing spinel catalysts through SCS procedure, in which Gly not only acts as the ligand to disperse Co$^{2+}$ and Al$^{3+}$, but also as fuel for the oxidation period. At 170–180 ℃, Co(NO$_3$)$_2$ with a lower decomposition temperature ignites Gly to instantly release its energy, rapidly increasing the system temperature and obtaining CoO$_x$/CoAl$_2$O$_4$ in a short period of time [46]. NH$_3$ and CO$_2$ released by Gly have brought abundant mesopores to the catalysts concurrently, and the N$_2$ adsorption-desorption isotherms of all samples show typical IV isotherm and H3 type hysteresis loop, with specific surface area of 45-70 m$^2$/g (Figs. 1a, S1 and Table S1). As shown in Fig. 1b-c, XRD was used to characterize the crystal structure of the catalysts. The diffraction peaks of unreduced sample Co/CoAl$_2$O$_4$-UR at 31.2°, 36.8°, 44.7°, 55.6°, 59.3° and 65.1° are well indexed to (220), (311), (400), (422), (511) and (440) of CoAl$_2$O$_4$ (PDF#70-0753). The almost overlapping peaks of CoAl$_2$O$_4$ and Co$_3$O$_4$ (PDF#42-1467) make it difficult to distinguish between the two phases, but the peak intensity ratio of 31.2° and 36.8° (I$_R$=I(31.2°)/I(36.8°)) can roughly reflect the content of CoAl$_2$O$_4$ and Co$_3$O$_4$ in the samples. As shown in Fig. S2 and Table S2, I$_R$ value of 0.38 between 0.34 (Co$_3$O$_4$) and 0.60 (CoAl$_2$O$_4$) indicates that Co$_3$O$_4$ and CoAl$_2$O$_4$ coexist in Co/CoAl$_2$O$_4$-UR catalyst. After the sample is reduced by H$_2$, I$_R$ progressively approaches the theoretical ratio of CoAl$_2$O$_4$ phase, indicating that Co$_3$O$_4$ is gradually reduced to Co (PDF#15-0806), while CoAl$_2$O$_4$ retains its diffraction peaks because of higher stability [31]. For Co/CoAl$_2$O$_4$-R400, part of Co$_3$O$_4$ is reduced to CoO and slight Co, resulting in a decrease in the content of Co$_3$O$_4$. When the reduction temperature rises to 500 ℃, almost all Co$_3$O$_4$ is reduced to simple substance, and the diffraction peak of CoAl$_2$O$_4$ at 44.7° has also shifted to the left, approaching the diffraction peak of Co at 44.2°(111). As the reduction temperature further increases to 600 ℃, the intensity of the diffraction peak at 44.2° enhances, corresponding to the generation of more Co. It is worth noting that no diffraction peak of Al$_2$O$_3$ (PDF#04-0880) appears in all samples, which further proves that Al exists in the form of CoAl$_2$O$_4$. After adjusting Gly content in the ingredients, the diffraction peaks do not shift, as evident in Fig. 1c. When increasing Co/Al ratio, 0.6Co/0.4Al-Co/CoAl$_2$O$_4$ exhibits a significant peak at 44.2°, indicating more Co on the surface. Unlike other samples, 0.4Co/0.6Al-Co/CoAl$_2$O$_4$ doesn't show a left shift of the peak at 44.7° after the same reduction process, which is attributed to the low Co/Al ratio resulting in fewer Co$_3$O$_4$ on the unreduced catalyst. The ICP results listed in Table S1 also support the above XRD analysis, with the Co/Al atomic ratio in all samples similar to the theoretical value.

SEM images are displayed in Figs. 2a and S3 to compare the morphology of different samples. Corresponding to the N$_2$ adsorption-desorption isotherms analysis results, all samples exhibit a layered stacking structure with abundant mesopores. In comparison with the unreduced sample Co/CoAl$_2$O$_4$-UR, the surfaces of the reduced samples show uniformly dispersed small particles with a diameter of about 20 nm, which is precisely the reduced Co nanoparticles. As the reduction temperature increases from 400 to 500 ℃, and then to 600 ℃, there is an apparent increase in Co nanoparticles on the surfaces of catalysts, consistent with the XRD results. Changing the ratio of Gly or Co/Al does not visibly affect the micro appearance of the catalysts, except for 0.4Co/0.6Al-Co/CoAl$_2$O$_4$, which shows fewer nanoparticles on its surface due to the lower Co doping amount. These SEM images completely coincide with the XRD analysis. As illustrated in Fig. S4, EDS spectroscopy elemental mapping of Co/CoAl$_2$O$_4$ clearly reveals the even distributions of Co, Al and O elements. TEM and HRTEM were conducted to observe the distribution of Co and CoAl$_2$O$_4$ on the surfaces of catalysts. Changing Co/Al ratio has little effect on the size of metal particles, and the Co particles on the surfaces of Co/CoAl$_2$O$_4$ (19.6 nm), 0.4Co/0.6Al-Co/CoAl$_2$O$_4$ (19.4 nm), and 0.6Co/0.4Al-Co/CoAl$_2$O$_4$ (18.8 nm) exhibit similar particle size distributions (Figs. 2b and S5). The HRTEM image
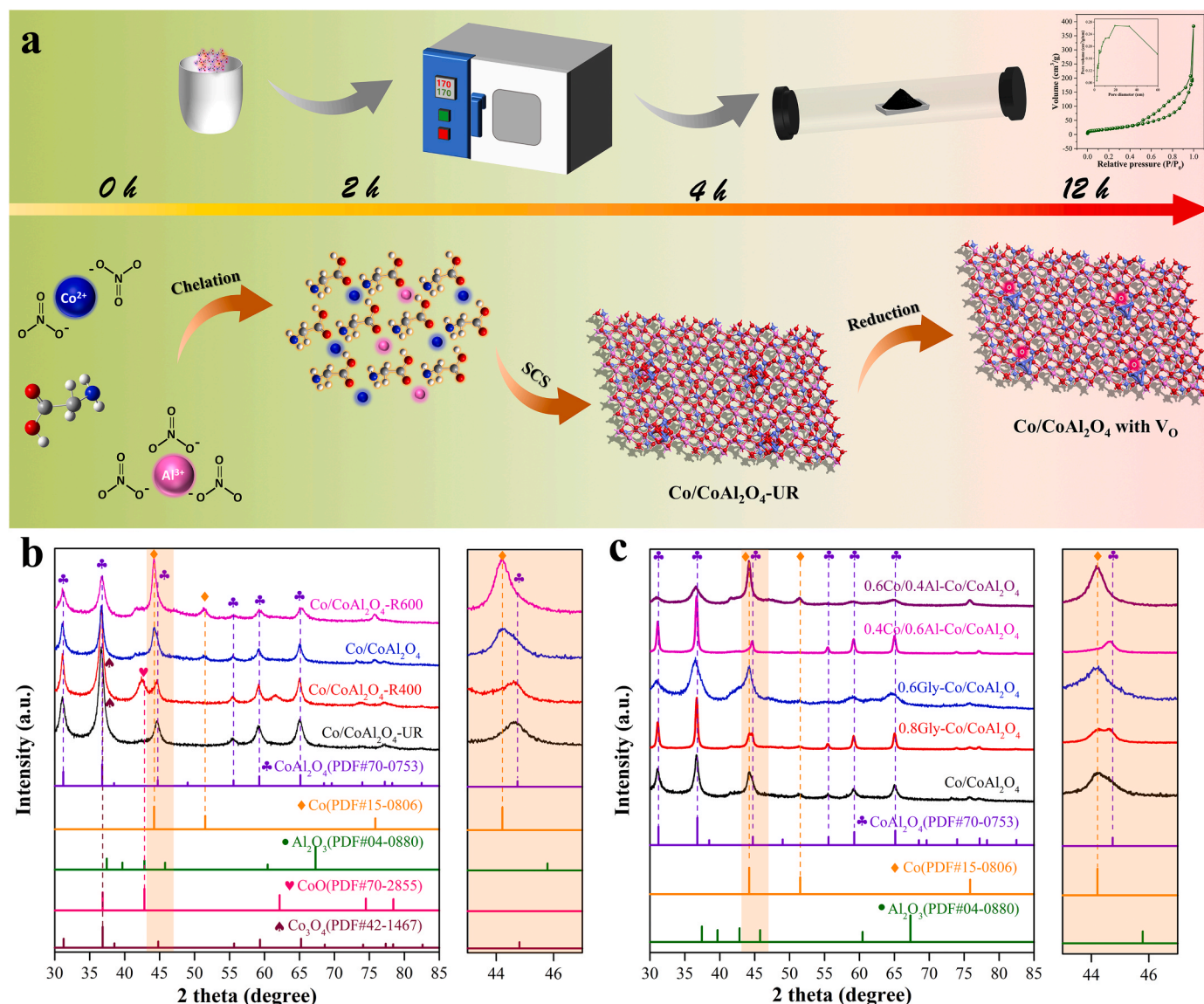
**Fig. 1.** (a) Schematic illustration for the synthesis of Co/CoAl$_2$O$_4$. (b) XRD patterns of catalysts reduced at different temperatures. (c) XRD patterns of catalysts with different Gly/Co/Al ratios.

and elemental mapping in Fig. 2d-e demonstrate that Co and Al are evenly distributed in the carrier, while the particles on the surface are metallic Co. The SAED pattern (Fig. 2f) shows that CoAl$_2$O$_4$ mainly exhibits (220), (311) and (440) facets, while Co mainly exhibits (111) and (200) facets. The SAED patterns of other samples (Fig. S6) show similar results, except for the unreduced sample Co/CoAl$_2$O$_4$-UR, which have only sparse Co particles on the surface (Fig. S5).

To investigate the effects of reduction temperature and Gly addition on the valence states of metals and coordination structures, XPS was employed and the results are shown in Fig. 2g-i. As the reduction temperature rises (Fig. 2g), Co$^{3+}$ (779.8 eV) is gradually converted into Co$^0$ (778.7 eV), and almost all of Co$^{3+}$ is reduced when the temperature reaches 500 °C. The more manifest satellite peaks confirm the above statement based on the fact that the satellite peak of Co$^{2+}$ is stronger than that of Co$^{3+}$ [37,47]. Notably, the XPS peaks of Co 2$p$ shift to higher binding energy concurrently, not only because Co$_3$O$_4$ is reduced, but also more oxygen vacancies are generated during the reduction process, increasing the electron density around Co [48]. It should be emphasized that the special electronic structure of Co makes the external electronic layer of Co$^{2+}$ be arranged in a full configuration, which is more stable than Co$^{3+}$ and possesses higher binding energy. There is no apparent

difference in the valence state of Co when the reduction temperature exceeds 500 °C. According to Fig. 2h and Table S3, the O 1 $s$ spectra can be decomposed into lattice oxygen (O$_l$), oxygen vacancy (O$_v$), and surface adsorbed oxygen species (O$_a$). When $n_{Gly}/(n_{Co}+n_{Al})$ drops from 0.8 to 0.6, the content of oxygen vacancies shows a trend of volcanic type changes. This can be explained as: Less Gly leads to the inability to reach higher combustion temperature during the combustion synthesis process, thereby reducing the content of oxygen vacancies; Excessive Gly may suppress Kirkendall effect, trigger fuel residue and is not conducive to the exposure of oxygen vacancies. The almost identical amounts of Co$^{2+}$ and Co$^0$ in 0.6Gly-Co/CoAl$_2$O$_4$, Co/CoAl$_2$O$_4$ and 0.8Gly-Co/-CoAl$_2$O$_4$ samples indicate that changing the proportion of Gly has little effect on the valence states of metals in the catalyst (Fig. 2i and Table S4). Compared with 0.6Gly-Co/CoAl$_2$O$_4$, the peak positions of Co$^{2+}$ in Co/CoAl$_2$O$_4$ and 0.8Gly-Co/CoAl$_2$O$_4$ both shift slightly higher by 0.2 eV, suggesting more pronounced charge transfers from vacancy oxygen to vicinal Co, consist with the analysis conclusion of O 1 $s$ spectra. As shown in Fig. 2j, EPR spectra were acquired to accurately quantify the surface oxygen vacancies of various catalysts. In accordance with XPS analysis results, oxygen vacancies at g= 2.003 augment in the order of 0.6Gly-Co/CoAl$_2$O$_4$ < 0.8Gly-Co/CoAl$_2$O$_4$ < Co/CoAl$_2$O$_4$. In
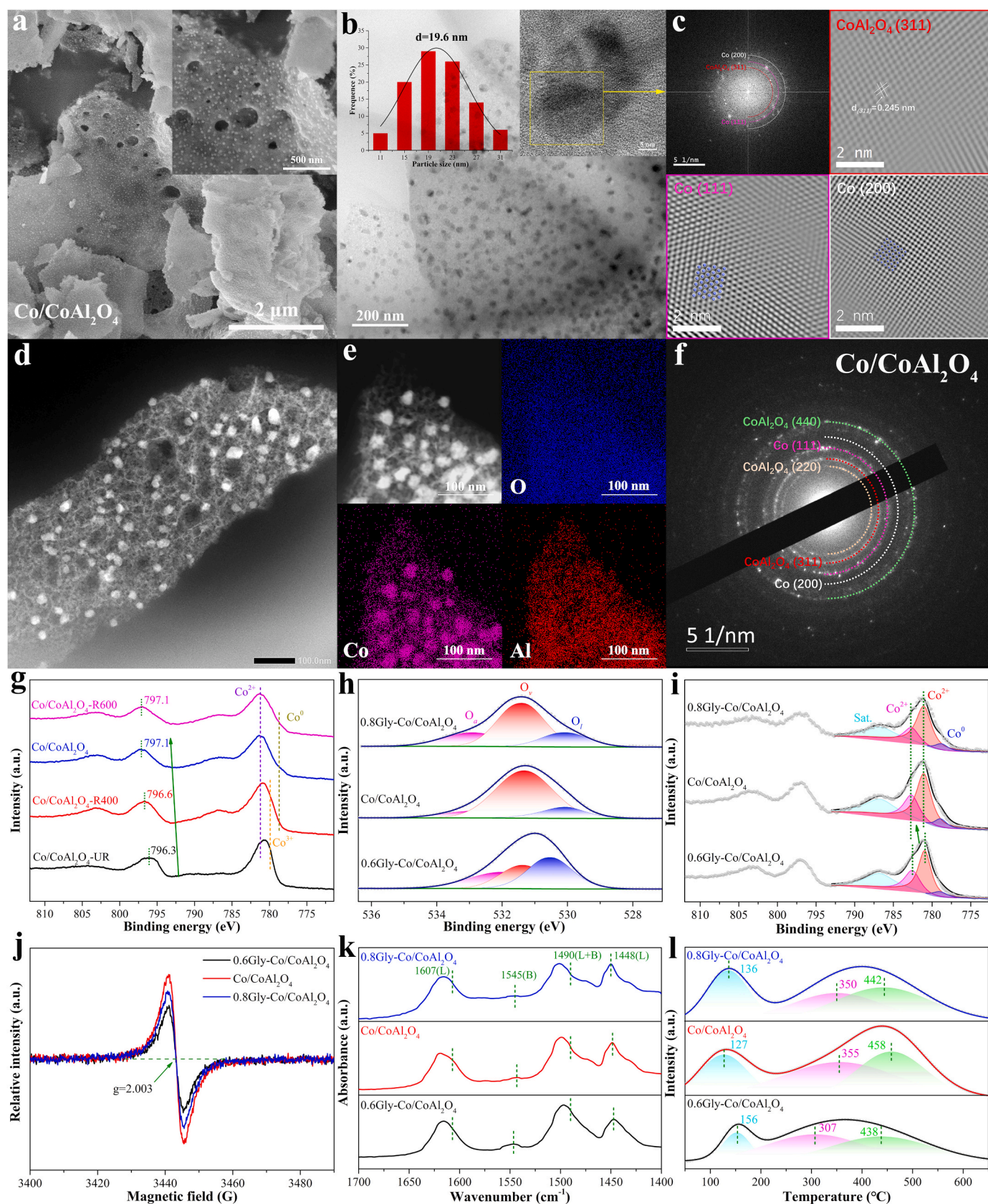
**Fig. 2.** (a) SEM image, (b) TEM image, (c) FFT image, (d) HRTEM image, (e) EDX mapping, and (f) SAED pattern of Co/CoAl$_2$O$_4$. (g) XPS spectra of Co 2$p$ for Co/CoAl$_2$O$_4$ reduced at different temperatures. XPS spectra of (h) O 1 $s$ and (i) Co 2$p$ for 0.6Gly-Co/CoAl$_2$O$_4$, Co/CoAl$_2$O$_4$ and 0.8Gly-Co/CoAl$_2$O$_4$. (j) ESR spectra, (k) Pyridine-DRIFT (200 ℃) and (l) H$_2$-TPD profiles of 0.6Gly-Co/CoAl$_2$O$_4$, Co/CoAl$_2$O$_4$ and 0.8Gly-Co/CoAl$_2$O$_4$.

order to determine whether the solution combustion synthesis process contributes to oxygen vacancies, the unreduced sample Co/CoAl$_2$O$_4$-UR was also characterized by EPR to shield the impact of the reduction procedure. Fig. S7 demonstrates that the initial combustion synthesis period first brings partial oxygen vacancies, which may originate from Kirkendall effect caused by the unbalanced diffusion rate of various materials, and facilitate the subsequent hydrogen spillover on the carrier [49–51]. Pyridine-DRIFT was carried out to compare the acidity of 0.6Gly-Co/CoAl$_2$O$_4$, Co/CoAl$_2$O$_4$ and 0.8Gly-Co/CoAl$_2$O$_4$ (Figs. 2k and S8). The peaks around 1448 and 1607 cm$^{-1}$ represent the adsorption of pyridine on Lewis acid sites, and the peak around 1545 cm$^{-1}$ corresponds to the adsorption of pyridine on Brønsted acid sites [31,52]. Regardless of the total acid content (200 °C) or strong acid content (350 °C), all three samples exhibit similar Lewis acidity and negligible Brønsted acidity, indicating that adjusting the amount of Gly will not significantly affect the acidity of the catalysts. Fig. 2l shows the H$_2$-TPD profiles of the samples, which fall into two regions: Low temperature peaks (<400 °C) belong to hydrogen chemisorbed (50–200 °C) and dissociated (200–400 °C) on Co particles, while high temperature peaks (>400 °C) represent hydrogen in subsurface layers or spillover hydrogen [31,53–55]. The stronger adsorption and dissociation capabilities of Co/CoAl$_2$O$_4$ for hydrogen promise its high hydrogenation activity, while the inferior hydrogen adsorption ability of 0.6Gly-Co/CoAl$_2$O$_4$ is not conducive to the hydrogenation reaction. Besides, the desorption peak at 400–550 °C attributed to spillover hydrogen appears in all samples, with Co/CoAl$_2$O$_4$ catalyst displaying the highest desorption temperature and desorption capacity, implying more oxygen vacancies in it [56]. By comparison, the spillover hydrogen of 0.8Gly-Co/CoAl$_2$O$_4$ and 0.6Gly-Co/CoAl$_2$O$_4$ decreases sequentially, consistent with the XPS and EPR results.

## 3.2. Catalytic performance

As presented in Fig. 3a-c, comparative experiments were implemented to optimize the reaction conditions to explore the effects of the ratio of Gly/Co/Al, and reduction temperature on catalytic performance. Under the same molar ratio of Co and Al, the yield of 2-MF first increases and then decreases as $n_{Gly}/(n_{Co}+n_{Al})$ increases from 0.5 to 0.9, presenting a typical volcanic curve, although these catalysts share almost the same conversion rate (Fig. 3a). Co/CoAl$_2$O$_4$ catalyst ($n_{Gly}/(n_{Co}+n_{Al}) = 0.7$) affords the best 2-MF yield of 97.2 %, while other catalysts relatively yield more FOL. Based on the above characterization analysis, merely changing the amount of Gly has low impact on the particle size and valence distribution of Co species, as well as acidic sites on the catalysts. The main difference between these catalysts lies in oxygen vacancies, and the trends of change in their catalytic activity and oxygen vacancies are completely consistent, highlighting the importance of oxygen vacancies. Locking $n_{Gly}/(n_{Co}+n_{Al})$ at the optimal value of 0.7 and adjusting the relative content of Co and Al, it is found that an excessive or insufficient proportion of $n_{Co}/n_{Al}$ is not conducive to improving catalytic performance (Fig. 3b). As analyzed by XRD and SEM, reducing the initial $n_{Co}/n_{Al}$ ratio significantly reduces the Co content on the surface of catalyst, which is crucial for activation of H$_2$, resulting in a 2-MF yield of only 38.2 % for 0.4Co/0.6Al-Co/CoAl$_2$O$_4$ ($n_{Co}/n_{Al} = 0.4/0.6$). Similarly, the inappropriate metal/metal oxide ratio caused by increasing the $n_{Co}/n_{Al}$ ratio also reduces the 2-MF yield of 0.6Co/0.4Al-Co/CoAl$_2$O$_4$ ($n_{Co}/n_{Al} = 0.6/0.4$) to 81.5 %. It can be seen that the $n_{Co}/n_{Al}$ ratio plays a vital impact on the catalytic activity, and equal moles of Co and Al become the optimal solution in this study. Subsequently, the optimal reduction temperature of the Co/CoAl$_2$O$_4$ catalyst was studied (Fig. 3c). Co/CoAl$_2$O$_4$-R400 catalyst reduced at 400 °C is in inferior position, as it not only fails to completely convert
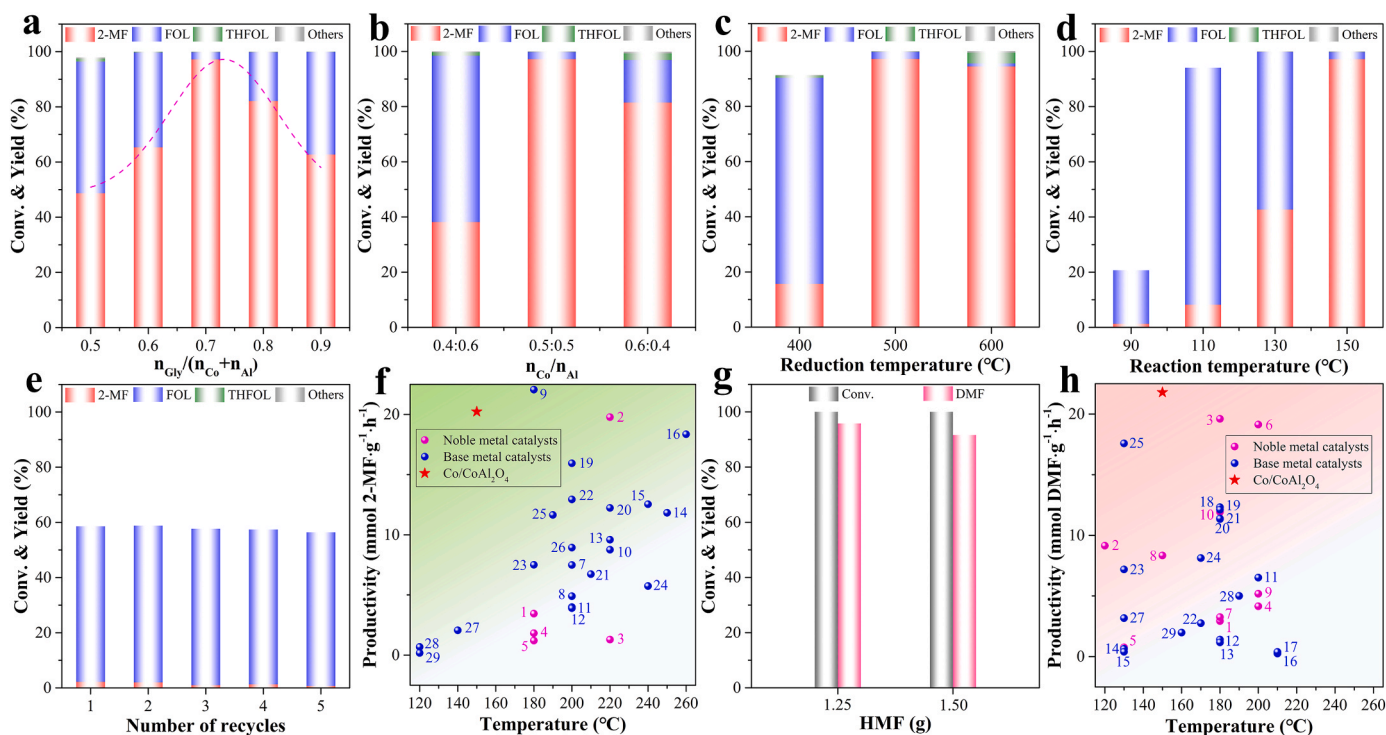


**Fig. 3.** Conversion and yield of FF hydrodeoxygenation over catalysts with (a) different $n_{Gly}/(n_{Co}+n_{Al})$ ratios, (b) different $n_{Co}/n_{Al}$ ratios, (c) different reduction temperatures (reaction condition: 1 g of FF, 0.1 g of catalyst, 19 g of ethanol, 1.5 MPa of H$_2$, 150 °C, 5 h). (d) Conversion and yield of FF hydrodeoxygenation over Co/CoAl$_2$O$_4$ at varying reaction temperatures (reaction condition: 1 g of FF, 0.1 g of Co/CoAl$_2$O$_4$, 19 g of ethanol, 1.5 MPa of H$_2$, 5 h). (e) Recyclability of the Co/CoAl$_2$O$_4$ catalyst (reaction condition: 1 g of FF, 0.035 g of Co/CoAl$_2$O$_4$, 19 g of ethanol, 1.5 MPa of H$_2$, 150 °C, 1 h). (f) Comparison of the productivity of the state-of-the-art catalysts for the hydrodeoxygenation of FF to 2-MF (Full data is shown in Table S5). (g) Conversion and yield of HMF hydrodeoxygenation over Co/CoAl$_2$O$_4$ at different HMF content (reaction condition: 0.1 g of Co/CoAl$_2$O$_4$, 19 g of ethanol, 1.5 MPa of H$_2$, 150 °C, 5 h). (h) Comparison of the productivity of the state-of-the-art catalysts for the hydrodeoxygenation of HMF to DMF (Full data is shown in Table S6).

furfural, but also produces mainly FOL instead of 2-MF. As stated in XRD, SEM and XPS sections, the lower reduction temperature endows the catalyst with insufficient Co on its surface, thereby limiting the catalytic activity. An excessively high reduction temperature also curtails the selectivity of the catalyst to 2-MF: Metal oxides are reported as the initiator of the cleavage of the side chains of FOL [27]. More Co on the surface enhances the adsorption and activation of $H_2$, accompanied by less exposure of metal oxides, which could hinder the removal of hydroxyl groups of FOL and promote the hydrogenation of unsaturated bonds on the furan ring. XRD and SEM results manifest more Co on $Co/CoAl_2O_4$-R600 compared with $Co/CoAl_2O_4$, hence it can be understood that the $Co/CoAl_2O_4$-R600 catalyst reduced at 600 ℃ yields more tetrahydrofurfuryl alcohol (THFOL). After determining the optimal ratio of Gly/Al/Co and reduction temperature, the reaction conditions of the optimum catalyst $Co/CoAl_2O_4$ were optimized. Fig. 3d shows that the yield of 2-MF increases with increasing reaction temperature from 90 to 150 ℃, and 150 ℃ is the optimal reaction temperature since almost all FF is converted to 2-MF. At 110 ℃, more than 90 % of FF can be converted into FOL and a small amount of 2-MF in 5 h, while only one fifth can be converted with the same catalyst when FOL is used as the substrate, hinting that the reaction energy barrier from FOL to 2-MF is higher than that from FF to FOL (Fig. S9). Fig. S10 manifests that the conversion of FF exceeds 90 % in one hour, and it can be completely converted in less than three hours. The yield of 2-MF increases continuously with the extension of reaction time, and it approaches 100 % after five hours of reaction.

As displayed in Fig. S11, the $Co/CoAl_2O_4$ catalyst exhibits superior stability with a stable 2-MF yield on full conversion of FF after five reaction cycles, while similar pore structure parameters demonstrate the steady morphology of the catalyst after multiple cycles. To further examine the cyclic stability of the catalyst, the reaction conditions were adjusted to maintain a low conversion of FF (Fig. 3e). It can be seen that FOL dominates the products, while the conversion of FF remains stable at 56–59 % after multiple cycles, which further confirms the good cyclic stability of the catalyst. The productivities of advanced catalysts converting FF to 2-MF in relevant studies are statistically shown in Fig. 3f and Table S5, in which $Co/CoAl_2O_4$ catalyst stands out with higher conversion efficiency under lower reaction temperature.

HMF, another biomass-derived platform chemical, can be converted into DMF through similar hydrodeoxygenation (Scheme S1), and thus it can also be used to evaluate the catalytic hydrogenation performance of the $Co/CoAl_2O_4$ catalyst [7,57]. Fig. 3g demonstrates that the $Co/CoAl_2O_4$ has efficient catalytic performance for HMF: When the initial mass of HMF is 1.25 g, the yield of DMF reaches 95.8 % with the HMF conversion of 100 % at 150 ℃ for 5 h, and it reaches 91.6 % even if the mass of HMF increases to 1.5 g. Similarly, the productivities of advanced catalysts converting HMF to DMF are statistically analyzed and shown in Fig. 3h and Table S6. The $Co/CoAl_2O_4$ catalyst still exhibits excellent catalytic performance, with the productivity of 21.79 mmol $DMF \cdot g^{-1} \cdot h^{-1}$ at 150 ℃.

### 3.3. DFT calculations

As the most easily exposed crystal planes, Co(111) and Co(200) facets were used to calculate the adsorption energy for $H_2$, respectively. As shown in Figs. 4a-c and S12–13, the adsorption of $H_2$ on the top, bridge, and hollow sites of Co surfaces is investigated in both vertical and parallel manners. Similar to the results reported in the literature, the parallel adsorption modes show significantly higher adsorption energy, which is also the most likely adsorption manner for $H_2$ on the catalyst surface [31]. Relatively, Co(200) facet exhibits stronger adsorption capacity than Co(111) facet, while it is reported that taking nitrates as precursors may expose more Co(200) facet, so as to facilitate the adsorption of $H_2$ [58].

To analyze the adsorption of FF and FOL on metal oxide carriers, $CoAl_2O_4(311)$ without oxygen vacancies and with oxygen vacancies

were constructed, and their optimized structures and Bader charges are shown in Fig. 4d-e. The electronegativity of O makes it get electrons from Co and Al, so its valence-shell electrons increase, whereas the valence-shell electrons of Co and Al decrease. After generating oxygen vacancies, adjacent Co ($\delta$, $\varepsilon$) and Al ($\gamma$) atoms are stripped of less charges, and the density of the electron cloud increases, thus enhancing the adsorption capacity of the support to the reactants, which may be one of the important reasons for the increased activity of $CoAl_2O_4$-$V_O$. FT-IR was used to probe the adsorption configuration of FF and FOL on the surfaces of catalysts. As given in Fig. 4f, the FT-IR absorption peaks of pure FF at 1673, 1567 and 1463 $cm^{-1}$ represent the C=O stretching vibration, C=C antisymmetric stretching vibration and furan ring breath, respectively [17,52,56,59]. The peaks of 1278 and 930 $cm^{-1}$ correspond to $C^4$-O symmetric stretching vibration and in-plane bending vibration, while the peaks of 1156 and 1080 $cm^{-1}$ represent $C^1$-O stretching vibration [52,59–61]. Most of the remaining peaks come from C-H in-plane bending vibration. After high-temperature adsorption, blowing and other pre-treatments, the FT-IR absorption spectra of FF adsorbed on 0.6Gly-$Co/CoAl_2O_4$, $Co/CoAl_2O_4$ and 0.8Gly-$Co/CoAl_2O_4$ notably differ. The peak corresponding to C=O stretching vibration shifts towards a lower wavenumber (1629 $cm^{-1}$), indicating that C=O is adsorbed and activated. Analogously, the peak at 1278 $cm^{-1}$ representing $C^4$-O symmetric stretching vibration moves to 1230 $cm^{-1}$, accompanied by an obvious decrease in peak intensity, and the peak at 930 $cm^{-1}$ representing $C^4$-O in-plane bending vibration nearly vanishes. In stark contrast, the peaks representing C=C stretching vibrations have not undergone any deviation. The above analysis proves that the furan ring of FF is adsorbed on the catalyst surface, not in a parallel adsorption manner, but highly likely in a vertical adsorption manner, allowing the O in the furan ring to combine with the catalyst. This different adsorption method from previous reports is likely related to the presence of oxygen vacancies, which will be demonstrated through DFT calculations in the following. The FT-IR spectra in Fig. 4g depict the changes in functional groups of FOL adsorbed on the surface of 0.6Gly-$Co/CoAl_2O_4$, $Co/CoAl_2O_4$ and 0.8Gly-$Co/CoAl_2O_4$. Unlike the changes in FF, only $C^5$-O shows a significant red shift in the FOL adsorbed on the catalyst surface, while the functional groups on the furan ring, including C=C and C-O-C, exhibit no apparent change [59]. This indicates that FOL is adsorbed obliquely or parallel on the catalyst surface, with the furan ring not bonded to the active sites on the surface. The adsorption configuration different from FF may owe something to the larger steric hindrance of the hydroxyl group in FOL than the O atom in the aldehyde group of FF, making it difficult for the hydroxyl group to insert around the oxygen vacancy. The structures of FF and FOL adsorbed on the surfaces of $CoAl_2O_4$ and $CoAl_2O_4$-$V_O$ were optimized grounded on FT-IR testing, and the corresponding adsorption energies were calculated. The same as FT-IR analysis results, the furan ring of FF is perpendicular to the surface of $CoAl_2O_4$-$V_O$, where the O atom of the furan ring is connected with the active site, and the O atom of the aldehyde group is filled in the oxygen vacancy (Fig. S14c). Relatively, FF is inclined to adsorb on the surface of $CoAl_2O_4$, with only the O atom of the aldehyde group connected with the catalyst (Fig. S14b). Compared with Al, Co combines less O and loses less charge. Moreover, Co has more valence electrons in its $d$ orbital as a transition metal, which facilitate the adsorption and activation of reactants. After the generation of oxygen vacancies, more coordination unsaturated Co appears on the surface, and the number of adjacent active sites increases, which provides a prerequisite for the change of the adsorption configuration of FF on the surface of $CoAl_2O_4$-$V_O$. Specifically, Co($\delta$) has more valence electrons than Co($\varepsilon$) after the occurrence of oxygen vacancies (seen in Fig. 4d), endowing Co($\delta$) with stronger adsorption capacity for the aldehyde group of FF, whilst the absence of O atom adjacent to Co($\delta$) weakens the steric hindrance of adsorbing the aldehyde group. Fig. S14d-e manifest that the presence of oxygen vacancies elongates the C=O of FF from 1.257 to 1.333 Å after the adsorption, which facilitates the subsequent hydrogenation step, and the higher charge of O atom ($\eta$) in FF-$CoAl_2O_4$-$V_O$ further testify this
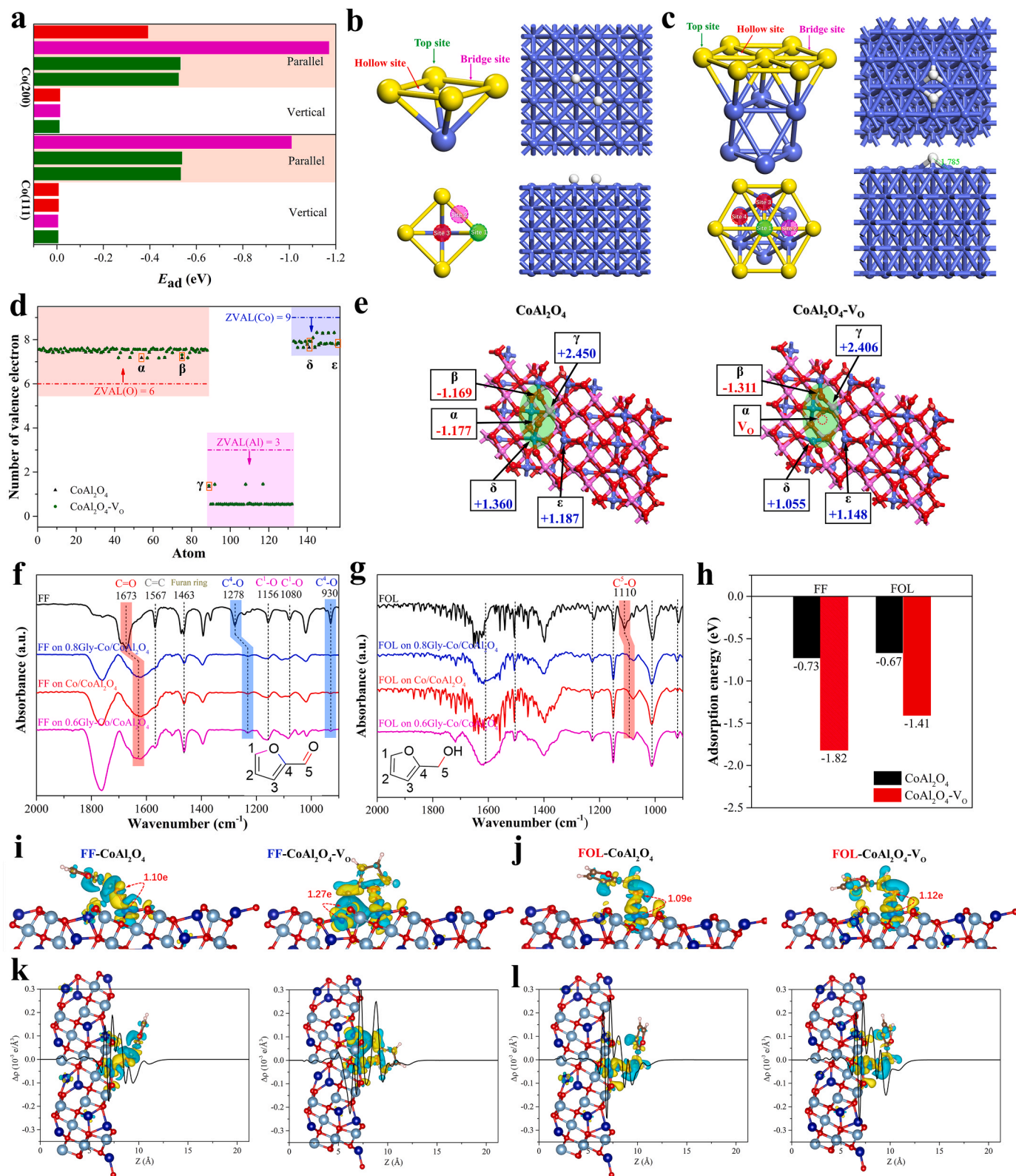
**Fig. 4.** (a) The adsorption energies of $H_2$ on Co (111) and Co (200) by DFT calculations. Optimal adsorption geometry of $H_2$ on (b) Co (200) and (c) Co (111). (e) Optimal adsorption geometries and (d) Bader charge analysis of $CoAl_2O_4$ and $CoAl_2O_4$-$V_O$. FT-IR absorption spectra of (f) FF and (g) FOL adsorbed on 0.6Gly-Co/$CoAl_2O_4$, Co/$CoAl_2O_4$ and 0.8Gly-Co/$CoAl_2O_4$. (h) The adsorption energies of FF and FOL on $CoAl_2O_4$ and $CoAl_2O_4$-$V_O$ by DFT calculations. The charge density difference of (i) FF and (j) FOL adsorbed on $CoAl_2O_4$ and $CoAl_2O_4$-$V_O$. Planar-averaged charge density difference along the vertical z-direction of (k) FF and (l) FOL adsorbed on $CoAl_2O_4$ and $CoAl_2O_4$-$V_O$.

viewpoint (Fig. S14a). Different from FF, FOL is adsorbed on the surfaces of $CoAl_2O_4$ and $CoAl_2O_4$-$V_O$ in parallel as a result of large steric hindrance of the hydroxyl group, and attached to the active site through hydroxyl (Fig. S15b-c). The existence of oxygen vacancies shortens the distance between the hydroxyl group of FOL and the active site of spinel, from 2.071 to 2.024 Å, which could be instrumental in hydrogenolysis process (Fig. S15d-e). As revealed in Fig. 4h, $CoAl_2O_4$-$V_O$ exhibits absolutely high adsorption capacity for both FF and FOL compared to $CoAl_2O_4$. To describe the adsorption energy of substrates on the catalyst surface under real reaction conditions, implicit solvent model was applied to the adsorption model accompanied by thermodynamic correction. It can be seen from Fig. S16 that the adsorption energy under real condition (ethanol, 423.15 K) slightly decreases (0.01–0.08 eV) compared to the ideal state (vacuum, 0 K), but the difference is not significant, indicating that it is feasible to ignore the effects of solvents and temperature on adsorption energy in this study, which is consistent with the result reported in the literature [5,62].

To further explain the difference in adsorption capacity caused by oxygen vacancies, the charge density difference and Bader charges of $CoAl_2O_4$ and $CoAl_2O_4$-$V_O$ after adsorbing reactants were investigated and displayed in Figs. 4i-j and S17: The O atoms in FF obtain different numbers of electrons from $CoAl_2O_4$ and $CoAl_2O_4$-$V_O$, with 1.10e from $CoAl_2O_4$ and 1.27e from $CoAl_2O_4$-$V_O$, which dovetails with the previous Bader charge analysis (Fig. 4d-e) and well explains the promoting effect of oxygen vacancies on the adsorption and activation of metal oxides to FF. Analogous electron transfer difference also occurs in the adsorption of FOL, manifesting the facilitation of oxygen vacancies on the adsorption and activation to FOL. In order to visualize the electron transfer between the metal oxide and the reactants, the plane-average electron difference in the z direction of the adsorption systems is calculated and plotted. As shown in Fig. 4k-l, the charge rearrangement mainly occurs on the surfaces of the metal oxides, and the charge accumulation ($\Delta\rho$ (z) > 0) appears between the active site Co and the O atom of the side chain of the reactant, while the electrons of the surface metal layer are consumed. Strikingly, oxygen vacancies exacerbate the electron transfer phenomenon of $CoAl_2O_4$ after adsorbing reactants, especially FF, which also confirms the facilitation of oxygen vacancies on the adsorption and activation of reactants on $CoAl_2O_4$.

For the hydrogenolysis of FOL to 2-MF, $H_2$ is dissociated into *H by Co particles and overflows to the active site Co of metal oxide, then combines with the adsorbed FOL. To elucidate the role of oxygen vacancies in promoting *H overflow towards the active centers where FOL is adsorbed, the densities of states (DOS) of $CoAl_2O_4$ and $CoAl_2O_4$-$V_O$ were investigated to analyze the $d$-band of the catalyst active center (Fig. 5a) [45]. Because of large exchange stabilization energy from strong spin polarization, spin down $d$-orbitals possess higher energy level than spin up $d$-orbitals, which means that spin down $d$-orbitals are closer to the Fermi level and more involved in the catalytic reaction [63, 64]. The $d$-band centers of spin down $d$-orbitals of $CoAl_2O_4$ and $CoAl_2O_4$-$V_O$ are marked in green lines, with values of $-0.215$ and $-0.305$, respectively. The presence of oxygen vacancies shifts the $d$-band center downwards, which weakens the binding of active site Co and *H. In the process of Co@CoO catalyst converting HMF to DMF, $H^{\delta-}$ attacks the C atom of $-CH_2$ is deemed as the rate determining step of 2,5-furandimethanol hydrogenolysis [37]. Similarly, by appropriately weakening the interaction between the active site Co of $CoAl_2O_4$-$V_O$ and *H, oxygen vacancies make it easier to combine *H with the activated FOL, which may lower the energy barrier of hydrogenolysis of FOL.

Grounded on the above analysis, the possible reaction path can be summarized as Fig. 5b: Firstly, oxygen vacancies enhance the adsorption and activation capacity of $CoAl_2O_4$ for FF, and change the adsorption configuration from tilted adsorption to vertical adsorption, with the O atom of the aldehyde group inserted into the oxygen vacancy and the O atom of the furan ring adsorbed on the Co active site. Subsequently, *H dissociated from $Co^0$ combines with the activated aldehyde group of FF to generate FOL, which desorbs from the catalyst then. For FOL, the
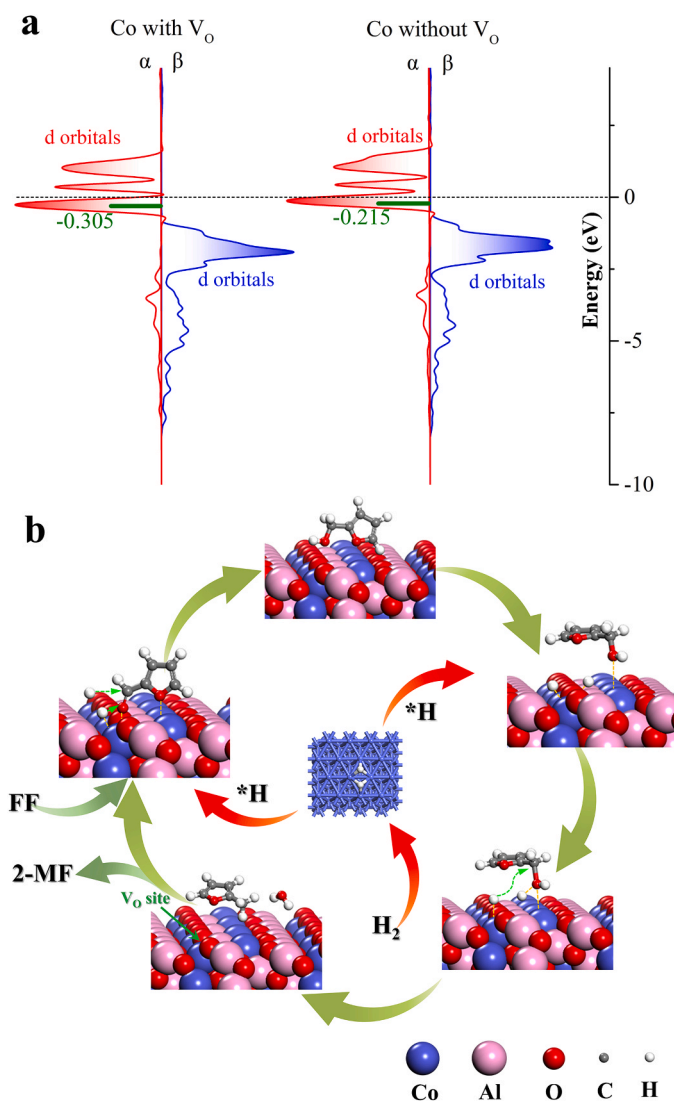
**Fig. 5.** (a) Projected electronic densities of states (pDOS) of $3d$ orbitals of active site Co on $CoAl_2O_4$ and $CoAl_2O_4$-$V_O$. (b) Plausible pathway for FF to 2-MF over Co/$CoAl_2O_4$ catalyst.

presence of oxygen vacancies does not alter its adsorption configuration on the surfaces of catalysts, but greatly improves its adsorption capacity. Sequentially, FOL undergoes C-OH scission, hydroxyl hydrogenation, water desorption, and methylene furan hydrogenation to obtain 2-MF. Oxygen vacancies appropriately attenuate the adsorption of vicinal active site Co to *H, thus promoting the spillover of *H desorbed from Co to activated FOL, presumably reducing the energy barrier from FOL to 2-MF.

## 4. Conclusion

A low-temperature solution combustion synthesis strategy has been constructed to prepare spinel catalysts to facilitate the upgrading of FF from biomass, in which the content of oxygen vacancies could be easily manipulated by adjusting the proportion of glycine in the ingredients. The $V_O$-rich Co/$CoAl_2O_4$ catalyst exhibits an excellent catalytic performance for the hydrodeoxygenation of FF with a 2-MF yield of over 97 % at 150 ℃ for 5 h, affording a productivity of 20.23 mmol 2-MF·$g^{-1}$·$h^{-1}$, rivalling the state-of-the-art catalysts to date. Oxygen vacancies contribute significantly to the ultra-high activity, which not only improve the adsorption capacity to FF by changing its adsorption geometry, but also promote the conversion of FOL to 2-MF by enhancing

hydrogen spillover. Also, the Co/CoAl$_2$O$_4$ catalyst shows the high productivity for the hydrodeoxygenation of HMF to DMF. This work sheds light on the rapid synthesis of spinel and the construction of defect engineering on catalysts, as well as designating a shortcut for the hydrogenation and hydrogenolysis of biomass chemicals.

## CRediT authorship contribution statement

**Yongwang Li:** Conceptualization, Investigation, Data curation, Formal analysis, Methodology, Writing – original draft. **Qi Shen:** Investigation, Writing – review & editing. **Yao Nian:** Data curation, Methodology. **Fumin Wang:** Supervision, Funding acquisition, Writing – review & editing. **Xubin Zhang:** Supervision, Funding acquisition, Writing – review & editing. **Zhengliang Zhang:** Writing – review & editing. **Changhao Bing:** Writing – review & editing. **Xiaolu Fan:** Writing – review & editing. **Rosine Ahishakiye:** Writing – review & editing.

## Declaration of Competing Interest

The authors declare that they have no known competing financial interests or personal relationships that could have appeared to influence the work reported in this paper.

## Data availability

Data will be made available on request.

## Acknowledgements

## Appendix A. Supporting information

Supplementary data associated with this article can be found in the online version at doi:10.1016/j.apcatb.2023.123529.

## References

[1] K. Zhang, Q. Meng, H. Wu, J. Yan, X. Mei, P. An, L. Zheng, J. Zhang, M. He, B. Han, Selective hydrodeoxygenation of aromatics to cyclohexanols over Ru single atoms supported on CeO$_2$, J. Am. Chem. Soc. 144 (2022) 20834–20846, https://doi.org/10.1021/jacs.2c08992.

[2] C. Wang, L. Wang, J. Zhang, H. Wang, J.P. Lewis, F.-S. Xiao, Product selectivity controlled by zeolite crystals in biomass hydrogenation over a palladium catalyst, J. Am. Chem. Soc. 138 (2016) 13756, https://doi.org/10.1021/jacs.6b04951.

[3] X. Zhao, F. Wang, X. Kong, R. Fang, Y. Li, Subnanometric Cu clusters on atomically Fe-doped MoO$_2$ for furfural upgrading to aviation biofuels, Nat. Commun. 13 (2022), 2591, https://doi.org/10.1038/s41467-022-30345-0.

[4] G. Gao, J. Remón, Z. Jiang, L. Yao, C. Hu, Selective hydrogenation of furfural to furfuryl alcohol in water under mild conditions over a hydrotalcite-derived Pt-based catalyst, Appl. Catal. B Environ. 309 (2022), 121260, https://doi.org/10.1016/j.apcatb.2022.121260.

[5] V. Ranaware, R.G. Kurniawan, D. Verma, S.K. Kwak, B.C. Ryu, J.W. Kang, J. Kim, Solvent-mediated selectivity control of furfural hydrogenation over a N-doped carbon-nanotube-supported Co/CoO$_x$ catalyst, Appl. Catal. B Environ. 318 (2022), 121838, https://doi.org/10.1016/j.apcatb.2022.121838.

[6] Y. Deng, R. Gao, L. Lin, T. Liu, X.-D. Wen, S. Wang, D. Ma, Solvent tunes the selectivity of hydrogenation reaction over alpha-MoC catalyst, J. Am. Chem. Soc. 140 (2018) 14481–14489, https://doi.org/10.1021/jacs.8b09310.

[7] W. Fang, A. Riisager, Recent advances in heterogeneous catalytic transfer hydrogenation/hydrogenolysis for valorization of biomass-derived furanic compounds, Green Chem. 23 (2021) 670–688, https://doi.org/10.1039/d0gc03931d.

[8] J. Tan, M. Jiang, K. Yu, Y. Song, W. Zhang, Q. Gao, Recent progress of Cu-based electrocatalysts for upgrading biomass-derived furanic compounds, Catal. Sci. Technol. 13 (2023) 2899–2921, https://doi.org/10.1039/d3cy00041a.

[9] N.S. Date, A.M. Hengne, K.W. Huang, R.C. Chikate, C.V. Rode, Single pot selective hydrogenation of furfural to 2-methylfuran over carbon supported iridium catalysts, Green Chem. 20 (2018) 2027–2037, https://doi.org/10.1039/c8gc00284c.

[10] K. Zhou, J. Chen, Y. Cheng, Z. Chen, S. Kang, Z. Cai, Y. Xu, J. Wei, Enhanced catalytic transfer hydrogenation of biomass-based furfural into 2-methylfuran over

[11] multifunctional Cu-Re bimetallic catalysts, ACS Sustain. Chem. Eng. 8 (2020) 16624–16636, https://doi.org/10.1021/acssuschemeng.0c06026.

[11] Z. Jin, X. Yi, L. Wang, S. Xu, C. Wang, Q. Wu, L. Wang, A. Zheng, F.-S. Xiao, Metal-acid interfaces enveloped in zeolite crystals for cascade biomass hydrodeoxygenation, Appl. Catal. B Environ. 254 (2019) 560–568, https://doi.org/10.1016/j.apcatb.2019.05.022.

[12] W. Geng, W. Li, L. Liu, J. Liu, L. Liu, X. Kong, Facile assembly of Cu-Cu$_2$O/N-reduced graphene oxide nanocomposites for efficient synthesis of 2-methylfuran, Fuel 259 (2020), 116267, https://doi.org/10.1016/j.fuel.2019.116267.

[13] J.B. Zhang, G.Q. Ding, Y. Jin, L.S. Wei, X.Q. Li, D.Y. Wang, Y.L. Zhu, Y.W. Li, Stabilizing the interfacial Cu$^0$-Cu$^+$ dual sites toward furfural hydrodeoxygenation to 2-methylfuran via fabricating nest-like copper phyllosilicate precursor, Fuel 337 (2023), 127212, https://doi.org/10.1016/j.fuel.2022.127212.

[14] W. Gong, Y. Lin, C. Chen, M. Al-Mamun, H.S. Lu, G. Wang, H. Zhang, H. Zhao, Nitrogen-doped carbon nanotube confined Co-N$_x$ sites for selective hydrogenation of biomass-derived compounds, Adv. Mater. 31 (2019), e1808341, https://doi.org/10.1002/adma.201808341.

[15] Z. Moravvej, F. Farshchi Tabrizi, M.R. Rahimpour, A. Behrad Vakylabad, Exploiting the potential of cobalt molybdenum catalyst in elevated hydrodeoxygenation of furfural to 2-methyl furan, Fuel 332 (2023), 126193, https://doi.org/10.1016/j.fuel.2022.126193.

[16] M. Kalong, P. Hongmanorom, S. Ratchahat, W. Koo-amornpattana, K. Faungnawakij, S. Assabumrungrat, A. Srifa, S. Kawi, Hydrogen-free hydrogenation of furfural to furfuryl alcohol and 2-methyl-furan over Ni and Co-promoted Cu/gamma-Al$_2$O$_3$ catalysts, Fuel Process. Technol. 214 (2021), 106721, https://doi.org/10.1016/j.fuproc.2020.106721.

[17] W. Liu, Y. Yang, L. Chen, E. Xu, J. Xu, S. Hong, X. Zhang, M. Wei, Atomically-ordered active sites in NiMo intermetallic compound toward low-pressure hydrodeoxygenation of furfural, Appl. Catal. B Environ. 282 (2021), 119569, https://doi.org/10.1016/j.apcatb.2020.119569.

[18] B. Seemala, C.M. Cai, C.E. Wyman, P. Christopher, Support induced control of surface composition in Cu-Ni/TiO$_2$ catalysts enables high yield co-conversion of HMF and furfural to methylated furans, ACS Catal. 7 (2017) 4070–4082, https://doi.org/10.1021/acscatal.7b01095.

[19] W. Yu, K. Xiong, N. Ji, M.D. Porosoff, J.G. Chen, Theoretical and experimental studies of the adsorption geometry and reaction pathways of furfural over FeNi bimetallic model surfaces and supported catalysts, J. Catal. 317 (2014) 253–262, https://doi.org/10.1016/j.jcat.2014.06.025.

[20] G. Giorgianni, S. Abate, G. Centi, S. Perathoner, S. van Beuzekom, S.-H. Soo-Tang, J.C. Van der Waal, Effect of the solvent in enhancing the selectivity to furan derivatives in the catalytic hydrogenation of furfural, ACS Sustain. Chem. Eng. 6 (2018) 16235–16247, https://doi.org/10.1021/acssuschemeng.8b03101.

[21] G. Kyriakou, M.B. Boucher, A.D. Jewell, E.A. Lewis, T.J. Lawton, A.E. Baber, H. L. Tierney, M. Flytzani-Stephanopoulos, E.C.H. Sykes, Isolated metal atom geometries as a strategy for selective heterogeneous hydrogenations, Science 335 (2012) 1209–1212, https://doi.org/10.1126/science.1215864.

[22] M. Audemar, C. Ciotonea, K. De Oliveira Vigier, S. Royer, A. Ungureanu, B. Dragoi, E. Dumitriu, F. Jerome, Selective hydrogenation of furfural to furfuryl alcohol in the presence of a recyclable cobalt/SBA-15 catalyst, ChemSusChem 8 (2015) 1885–1891, https://doi.org/10.1002/cssc.201403398.

[23] T.P. Sulmonetti, B. Hu, Z. Ifkovits, S. Lee, P.K. Agrawal, C.W. Jones, Vapor phase hydrogenolysis of furanics utilizing reduced cobalt mixed metal oxide catalysts, ChemCatChem 9 (2017) 1815–1823, https://doi.org/10.1002/cctc.201700228.

[24] C. Nguyen-Huy, J. Lee, J.H. Seo, E. Yang, J. Lee, K. Choi, H. Lee, J.H. Kim, M. S. Lee, S.H. Joo, J.H. Kwak, J.H. Lee, K. An, Structure-dependent catalytic properties of mesoporous cobalt oxides in furfural hydrogenation, Appl. Catal. A Gen. 583 (2019), 117125, https://doi.org/10.1016/j.apcata.2019.117125.

[25] R. Ahishakiye, F. Wang, X. Zhang, M. Sun, Y. Zhai, Y. Liu, Y. Wu, M. Li, M. Li, Q. Zhang, Novel noble metal-free and recyclable Co-CoO$_x$-FeNiCo/γ-Al$_2$O$_3$ catalyst for selective hydrogenation of 5-hydroxymethylfurfural to 2,5-dimethylfuran or 2,5-Bis(hydroxymethyl)furan, Chem. Eng. J. 450 (2022), 138187, https://doi.org/10.1016/j.cej.2022.138187.

[26] J. Chen, W. Sun, Y. Wang, W. Fang, Performant Au hydrogenation catalyst cooperated with Cu-doped Al$_2$O$_3$ for selective conversion of furfural to furfuryl alcohol at ambient pressure, Green Energy Environ. 6 (2021) 546–556, https://doi.org/10.1016/j.gee.2020.05.005.

[27] M.J. Gilkey, P. Panagiotopoulou, A.V. Mironenko, G.R. Jenness, D.G. Vlachos, B. Xu, Mechanistic insights into metal lewis acid-mediated catalytic transfer hydrogenation of furfural to 2-methylfuran, ACS Catal. 5 (2015) 3988–3994, https://doi.org/10.1021/acscatal.5b00586.

[28] M.J. Islam, M. Granollers Mesa, A. Osatiashtiani, J.C. Manayil, M.A. Isaacs, M. J. Taylor, S. Tsatsos, G. Kyriakou, PdCu single atom alloys supported on alumina for the selective hydrogenation of furfural, Appl. Catal. B Environ. 299 (2021), 120652, https://doi.org/10.1016/j.apcatb.2021.120652.

[29] X. Chang, A.F. Liu, B. Cai, J.Y. Luo, H. Pan, Y.B. Huang, Catalytic transfer hydrogenation of furfural to 2-methylfuran and 2-methyltetrahydrofuran over bimetallic copper-palladium catalysts, ChemSusChem 9 (2016) 3330–3337, https://doi.org/10.1002/cssc.201601122.

[30] H. Du, H. Guo, K. Wang, X. Du, B.A. Beshiwork, S. Sun, Y. Luo, Q. Liu, T. Li, X. Sun, Durable electrocatalytic reduction of nitrate to ammonia over defective pseudobrookite Fe$_2$TiO$_5$ nanofibers with abundant oxygen vacancies, Angew. Chem. 62 (2023), e202215782, https://doi.org/10.1002/ange.202215782.

[31] R.G. Kurniawan, N. Karanwal, J. Park, D. Verma, S.K. Kwak, S.K. Kim, J. Kim, Direct conversion of furfural to 1,5-pentanediol over a nickel-cobalt oxide-alumina trimetallic catalyst, Appl. Catal. B Environ. 320 (2023), 121971, https://doi.org/10.1016/j.apcatb.2022.121971.

[32] Y. Cao, D. Zheng, F. Zhang, J. Pan, C. Lin, Layered double hydroxide (LDH) for multi-functionalized corrosion protection of metals: a review, J. Mater. Sci. Technol. 102 (2022) 232–269, https://doi.org/10.1016/j.jmst.2021.05.078.

[33] Y. Wang, J. Mi, Z.-S. Wu, Recent status and challenging perspective of high entropy oxides for chemical catalysis, Chem. Catal. 2 (2022) 1624–1656, https://doi.org/10.1016/j.checat.2022.05.003.

[34] C.T. Campbell, C.H. Peden, Oxygen vacancies and catalysis on ceria surfaces, Science 309 (2005) 713–714, https://doi.org/10.1126/science.1113955.

[35] L. Zhang, H. Jang, H. Liu, M.G. Kim, D. Yang, S. Liu, X. Liu, J. Cho, Sodium-decorated amorphous/crystalline RuO$_2$ with rich oxygen vacancies: a robust pH-universal oxygen evolution electrocatalyst, Angew. Chem. 60 (2021) 18821–18829, https://doi.org/10.1002/ange.202106631.

[36] Y. Zhao, C. Chang, F. Teng, Y. Zhao, G. Chen, R. Shi, G.I.N. Waterhouse, W. Huang, T. Zhang, Defect-engineered ultrathin δ-MnO$_2$ nanosheet arrays as bifunctional electrodes for efficient overall water splitting, Adv. Energy Mater. 7 (2017), 1700005, https://doi.org/10.1002/aenm.201700005.

[37] S. Xiang, L. Dong, Z.Q. Wang, X. Han, L.L. Daemen, J. Li, Y. Cheng, Y. Guo, X. Liu, Y. Hu, A.J. Ramirez-Cuesta, S. Yang, X.Q. Gong, Y. Wang, A unique Co@CoO catalyst for hydrogenolysis of biomass-derived 5-hydroxymethylfurfural to 2,5-dimethylfuran, Nat. Commun. 13 (2022), 3657, https://doi.org/10.1038/s41467-022-31362-9.

[38] W. Cao, G.J. Xia, Z. Yao, K.H. Zeng, Y. Qiao, Y.G. Wang, Aldehyde hydrogenation by Pt/TiO$_2$ catalyst in aqueous phase: synergistic effect of oxygen vacancy and solvent water, JACS Au 3 (2023) 143–153, https://doi.org/10.1021/jacsau.2c00560.

[39] Kresse, Furthmuller, Efficient iterative schemes for ab initio total-energy calculations using a plane-wave basis set, Phys. Rev. B Condens. Matter 54 (1996) 11169–11186, https://doi.org/10.1103/PhysRevB.54.11169.

[40] Perdew, Burke, Ernzerhof, Generalized gradient approximation made simple, Phys. Rev. Lett. 77 (1996) 3865–3868, https://doi.org/10.1103/PhysRevLett.77.3865.

[41] G. Kresse, D. Joubert, From ultrasoft pseudopotentials to the projector augmented-wave method, Phys. Rev. B 59 (1999) 1758–1775, https://doi.org/10.1103/PhysRevB.59.1758.

[42] J.F.G. Kresse, Efficiency of ab-initio total energy calculations for metals and semiconductors using a plane-wave basis set, Comput. Mater. Sci. (1) (1996) 15–50, https://doi.org/10.1016/0927-0256(96)00008-0.

[43] K. Mathew, V.S.C. Kolluru, S. Mula, S.N. Steinmann, R.G. Hennig, Implicit self-consistent electrolyte model in plane-wave density-functional theory, J. Chem. Phys. 151 (2019), 234101, https://doi.org/10.1063/1.5132354.

[44] K. Mathew, R. Sundararaman, K. Letchworth-Weaver, T.A. Arias, R.G. Hennig, Implicit solvation model for density-functional study of nanocrystal surfaces and reaction pathways, J. Chem. Phys. 140 (2014), 084106, https://doi.org/10.1063/1.4865107.

[45] V. Wang, N. Xu, J.-C. Liu, G. Tang, W.-T. Geng, VASPKIT: A user-friendly interface facilitating high-throughput computing and analysis using VASP code, Comput. Phys. Commun. 267 (2021), 108033, https://doi.org/10.1016/j.cpc.2021.108033.

[46] A.V. Saghir, S.M. Beidokhti, J.V. Khaki, A. Salimi, One-step synthesis of single-phase (Co, Mg, Ni, Cu, Zn) O High entropy oxide nanoparticles through SCS procedure: thermodynamics and experimental evaluation, J. Eur. Ceram. Soc. 41 (2021) 563–579, https://doi.org/10.1016/j.jeurceramsoc.2020.08.044.

[47] D. Li, Q. Liu, C. Zhu, H. Wang, C. Cui, C. Wang, L. Ma, Selective hydrogenolysis of 5-hydroxymethylfurfural to 2,5-dimethylfuran over Co$_3$O$_4$ catalyst by controlled reduction, J. Energy Chem. 30 (2019) 34–41, https://doi.org/10.1016/j.jechem.2018.03.008.

[48] R. Tu, K. Liang, Y. Sun, Y. Wu, W. Lv, C.Q. Jia, E. Jiang, Y. Wu, X. Fan, B. Zhang, Q. Lu, B. Zhang, X. Xu, Ultra-dilute high-entropy alloy catalyst with core-shell structure for high-active hydrogenation of furfural to furfuryl alcohol at mild temperature, Chem. Eng. J. 452 (2023) 139526, https://doi.org/10.1016/j.cej.2022.139526.

[49] Z.W. Wei, H.J. Wang, C. Zhang, K. Xu, X.L. Lu, T.B. Lu, Reversed charge transfer and enhanced hydrogen spillover in platinum nanoclusters anchored on titanium oxide with rich oxygen vacancies boost hydrogen evolution reaction, Angew. Chem. 60 (2021) 16622–16627, https://doi.org/10.1002/anie.202104856.

[50] C. Mao, J. Wang, Y. Zou, G. Qi, J.Y. Yang Loh, T. Zhang, M. Xia, J. Xu, F. Deng, M. Ghoussoub, N.P. Kherani, L. Wang, H. Shang, M. Li, J. Li, X. Liu, Z. Ai, G. A. Ozin, J. Zhao, L. Zhang, Hydrogen spillover to oxygen vacancy of TiO$_{2-x}$H$_y$/Fe: breaking the scaling relationship of ammonia synthesis, J. Am. Chem. Soc. 142 (2020) 17403–17412, https://doi.org/10.1021/jacs.0c06118.

[51] D. Ji, L. Fan, L. Tao, Y. Sun, M. Li, G. Yang, T.Q. Tran, S. Ramakrishna, S. Guo, The Kirkendall effect for engineering oxygen vacancy of hollow Co$_3$O$_4$ nanoparticles toward high-performance portable zinc-air batteries, Angew. Chem. 58 (2019) 13840–13844, https://doi.org/10.1002/anie.201908736.

[52] Q. Wang, J. Feng, L. Zheng, B. Wang, R. Bi, Y. He, H. Liu, D. Li, Interfacial structure-determined reaction pathway and selectivity for 5-(hydroxymethyl) furfural hydrogenation over Cu-based catalysts, ACS Catal. 10 (2019) 1353–1365, https://doi.org/10.1021/acscatal.9b03630.

[53] S. Velu, S. Gangwal, Synthesis of alumina supported nickel nanoparticle catalysts and evaluation of nickel metal dispersions by temperature programmed desorption, Solid State Ion. 177 (2006) 803–811, https://doi.org/10.1016/j.ssi.2006.01.031.

[54] J.W. Curtis Conner, John L. Falconer, Spillover in heterogeneous catalysis, Chem. Rev. 95 (1995) 759–788, https://doi.org/10.1021/cr00035a014.

[55] S. Xia, L. Zheng, W. Ning, L. Wang, P. Chen, Z. Hou, Multiwall carbon nanotube-pillared layered Cu$_{0.4}$/Mg$_{5.6}$Al$_2$O$_{8.6}$: an efficient catalyst for hydrogenolysis of glycerol, J. Mater. Chem. A 1 (2013) 11548, https://doi.org/10.1039/c3ta12819a.

[56] T. Xiao, X. Liu, G. Xu, Y. Zhang, Phase tuning of ZrO$_2$ supported cobalt catalysts for hydrodeoxygenation of 5-hydroxymethylfurfural to 2,5-dimethylfuran under mild conditions, Appl. Catal. B Environ. 295 (2021), 120270, https://doi.org/10.1016/j.apcatb.2021.120270.

[57] Y. Jing, Y. Guo, Q. Xia, X. Liu, Y. Wang, Catalytic production of value-added chemicals and liquid fuels from lignocellulosic biomass, Chem 5 (2019) 2520–2546, https://doi.org/10.1016/j.chempr.2019.05.022.

[58] L. Wu, B. Li, Y. Li, X. Fan, F. Zhang, G. Zhang, Q. Xia, W. Peng, Preferential growth of the cobalt (200) facet in Co@N-C for enhanced performance in a Fenton-like reaction, ACS Catal. 11 (2021) 5532–5543, https://doi.org/10.1021/acscatal.1c00701.

[59] Y. Zhu, W. Zhao, J. Zhang, Z. An, X. Ma, Z. Zhang, Y. Jiang, L. Zheng, X. Shu, H. Song, X. Xiang, J. He, Selective activation of C-OH, C-O-C, or C≡C in furfuryl alcohol by engineered pt sites supported on layered double oxides, ACS Catal. 10 (2020) 8032–8041, https://doi.org/10.1021/acscatal.0c01276.

[60] M. Rogojerov, G. Keresztury, B. Jordanov, Vibrational spectra of partially oriented molecules having two conformers in nematic and isotropic solutions: furfural and 2-chlorobenzaldehyde, Spectrochim. Acta A Mol. Biomol. Spectrosc. 61 (2005) 1661–1670, https://doi.org/10.1016/j.saa.2004.11.043.

[61] Z. Tong, X. Li, J. Dong, R. Gao, Q. Deng, J. Wang, Z. Zeng, J.-J. Zou, S. Deng, Adsorption configuration-determined selective hydrogenative ring opening and ring rearrangement of furfural over metal phosphate, ACS Catal. 11 (2021) 6406–6415, https://doi.org/10.1021/acscatal.0c05497.

[62] Y. Mei, N.A. Deskins, An evaluation of solvent effects and ethanol oxidation, Phys. Chem. Chem. Phys. 23 (2021) 16180–16192, https://doi.org/10.1039/d1cp00630d.

[63] G. Gao, E.R. Waclawik, A. Du, Computational screening of two-dimensional coordination polymers as efficient catalysts for oxygen evolution and reduction reaction, J. Catal. 352 (2017) 579–585, https://doi.org/10.1016/j.jcat.2017.06.032.

[64] J.C. Liu, X.L. Ma, Y. Li, Y.G. Wang, H. Xiao, J. Li, Heterogeneous Fe$_3$ single-cluster catalyst for ammonia synthesis via an associative mechanism, Nat. Commun. 9 (2018), 1610, https://doi.org/10.1038/s41467-018-03795-8.